Twin–twin interactions in magnesium

Qin Yu [a,b], Jian Wang [b,*], Yanyao Jiang [a,*], Rodney J. McCabe [b], Nan Li [c],
Carlos N. Tomé [b]

[a] *Department of Mechanical Engineering, University of Nevada, Reno, Reno, NV 89557, USA*
[b] *MST-8, Los Alamos National Laboratory, Los Alamos, NM 87545, USA*
[c] *MPA-CINT, Los Alamos National Laboratory, Los Alamos, NM 87545, USA*

Abstract

When twin variants interact, TTBs form and consequently affect twinning and detwinning processes. In this paper, we study twin–twin interactions by combining experimental observations and theoretical analysis. Mg single crystals are cyclically loaded in $[0001]$ and $[10\bar{1}0]$ directions, respectively. Experimental characterization reveals the character of the twin–twin boundary and three kinds of twin–twin structures: a quilted-looking twin structure consisting of twins arrested at other twin boundaries, an "apparent crossing" twin structure which links twins impinging independently on each side of twin lamella and a double twin structure that results from secondary twins being nucleated at twin–twin interfaces. According to their crystallography, twin–twin interactions are classified into Type I for two twin variants sharing the same $\langle 11\bar{2}0 \rangle$ zone axis and Type II for two twins with different zone axes. For Type I twin–twin interactions, one twin does not transmit across the twin boundary and into the other twin. For Type II twin–twin interactions, one twin can transmit into the other only under some special loading conditions. In most cases twin transmission does not occur but, instead, twin–twin boundaries form that contain boundary dislocations. For Type I twin–twin interactions, the twin–twin boundary is a low angle tilt boundary with the habit plane being either the basal or the prismatic plane. For Type II twin–twin interactions, the twin–twin boundary is a high index crystallographic plane according to geometry analysis. Twin–twin boundary dislocations can be inferred by reactions of twinning dislocations associated with the two twin variants. An "apparent crossing" twin structure is thus a consequence of twin–twin boundary formation. Under reversed loading, detwinning is hindered because of the energetically unfavorable dissociation of boundary dislocations. Most interestingly, secondary twinning is activated at Type II twin–twin boundaries under reversed loading.
Published by Elsevier Ltd. on behalf of Acta Materialia Inc.

1. Introduction

Magnesium (Mg) and its alloys are the lightest structural metals and have the attraction of reducing vehicle weight and thereby increasing vehicle efficiency. However, Mg and Mg alloys exhibit very limited formability at room temperature because the hexagonal-close-packed (hcp) structure has a limited number of slip systems. As a consequence, twinning and detwinning commonly play a critical role during plastic deformation of polycrystalline aggregates. Twinning/detwinning has been characterized using in situ meso- and macro-scale techniques such as optical microscopy [1–3], acoustic emission [4,5] and neutron diffraction [6,7]. In parallel, materials modeling tools at meso- and macro-scales have been developed to quantitatively simulate the contribution of twinning/detwinning to plastic deformation and texture evolution [8–14].

* Corresponding authors. Tel.: +1 505 667 1238 (J. Wang), +1 775 784 4510 (Y. Jiang).

E-mail addresses: wangj6@lanl.gov (J. Wang), yjiang@unr.edu (Y. Jiang).

Characterization of microstructures related to twinning/detwinning, such as twin boundaries, dislocation–twin boundary interactions and twin–twin interactions, has provided insight into understanding microstructural features and the role of twinning/detwinning in mechanical deformation, as well advancing the development of materials modeling tools at meso- and macro-scales [8–14]. The combination of in situ/ex situ scanning electron microscopy (SEM) [15–18] and transmission electron microscopy (TEM) [19–23] with atomistic simulations [24–34], has shown that $\{10\bar{1}2\}$ twin boundaries are serrated and are formed by $\{10\bar{1}2\}$ coherent twin boundary (CTB) and prismatic‖basal boundaries (PB) [22]. Correspondingly, $\{10\bar{1}2\}$ twin boundaries can heavily deviate from the twinning plane [19]. The formation of such serrated twin boundaries was ascribed to dislocation–twin boundary interactions [31]. Thus, propagation of twins is accomplished through the migration of CTBs and PBs. In addition, the migration of a PB boundary can result in the emission of partial dislocations on the basal plane, forming stacking faults as evidenced in high resolution TEM [22]. These microstructural features can be related to twinning-induced hardening [3].

Dislocation–twin boundary interactions in hcp metals have been reported extensively. It has been shown that when a mixed edge/screw basal dislocation interacts with a twin boundary, twinning dislocations (TDs) and residual defects are produced at the TB [29–34]. At $\{\bar{1}011\}$ and $\{\bar{1}013\}$ TBs, only one TD can be created by the dissociation of a mixed dislocation [28]. However, the dissociation of a mixed basal dislocation at the $\{\bar{1}012\}$ TB can generate multiple TDs [34]. As TDs glide along the TB, the TB migrates. This can be a mechanism for expanding or contracting the twin domain. However, the interaction of one screw basal dislocation with a TB does not lead to TB migration because it cross-slips through the TB [34].

Twin–twin interactions in hcp metals were first studied by Reed-Hill and Buchanan in the 1960s [35]. Microstructures in association with twin–twin interactions were found to correlate with mechanical hardening [36–38]. Yu et al. [3] observed that twin–twin junctions resulting from twin–twin interactions could retard detwinning. The retardation behavior was ascribed to the unfavorable dissociation of twin–twin boundary (TTB) dislocations. Crossing-like twin structure has been observed in hcp metals, such as zinc [39], zirconium [35] and magnesium [40,41]. For a crossing-like twin structure, Cahn proposed a continuity condition based on the observed structure in α-uranium [42], stating that two constraints are required for the crossing-like twin–twin intersection: (1) the traces of the crossing twin and the secondary twin in the K_1 plane of the crossed twin must be parallel; (2) the direction and magnitude of the twinning shear must be identical in the crossing and secondary twins. However, the second constraint condition had been questioned when it is applied to twin–twin intersections in hcp metals [39–41]. Roberts and Partridge [40] experimentally characterized TTBs

between two $\{10\bar{1}2\}$ twin variants in Mg, where the boundaries were identified as a common interface bisecting two twinning planes. They pointed out that a local rotation of the twin lattice in the vicinity of the contact site could be the result of a stress relaxation process across the contact interface accompanying the formation of the common interfaces between the two twins.

In this paper, we revisit twin–twin interactions and address critical issues regarding interaction structures and twin transmission. We perform two cyclic loading tests in Mg single crystals along the $[0001]$ and $[10\bar{1}0]$ directions, respectively. In the two tests, $\{10\bar{1}2\}$ twinning and detwinning are the major deformation modes, offering the best situation to study twin–twin interactions. Three typical twin–twin structures are investigated: a quilted-looking twin structure consisting of twins arrested at other twin boundaries, an "apparent crossing" twin structure which links twins impinging independently on each side of twin lamella and a double twin structure that results from secondary twins being nucleated at twin–twin interfaces. Combining experimental characterization and theoretical dislocation analysis, we address the critical twin–twin interaction issues. The analytical method used and the major conclusions derived here for Mg can be straightforwardly applied to other metals/alloys with hcp structures.

2. Twin–twin interactions

2.1. Classification of twin–twin interactions

The $\{10\bar{1}2\}\langle\bar{1}011\rangle$ twin in hcp structures has six crystallographically equivalent variants, denoted here by the symbol T_i ($i = 1$–6). Labels increase by a counter-clockwise rotation about the c-axis (Fig. 1a). Three pairs of twin–twin interactions are crystallographically different, $T_1 \leftrightarrow T_2$, $T_1 \leftrightarrow T_3$ and $T_1 \leftrightarrow T_4$, as illustrated in Fig. 1b–d. The symbols "$T_i \leftrightarrow T_j$" denote an incoming twin T_i encountering twin T_j, and vice versa.

For $T_1 \leftrightarrow T_4$ twin–twin interaction pairs, the intersection line is parallel to the $[1\bar{2}10]$ direction (an a-axis). The c-axis misorientation angle between T_1 and T_4 is 7.40° for Mg. The $T_1 \leftrightarrow T_4$ twin–twin interaction is referred to as Type I co-zone twin–twin interaction. For $T_1 \leftrightarrow T_2$ and $T_1 \leftrightarrow T_3$ twin–twin interactions, the intersection lines are along $[\bar{2}\bar{2}43]$ and $[02\bar{2}1]$ directions, respectively. The c-axis misorientation angles about these axes are 79.98° for $T_1 \leftrightarrow T_2$ twin pair and 34.73° for $T_1 \leftrightarrow T_3$ twin pair, respectively. Since the two twin pairs do not share an a-axis, their interactions are referred to as Type II twin–twin interactions, with Type II(a) for $T_1 \leftrightarrow T_2$ and Type II(b) for $T_1 \leftrightarrow T_3$.

2.2. Do twins cross each other?

In this section we discuss the feasibility of twin transmission when an impinging twin crosses another twin through a secondary twinning path within the crossed twin. To
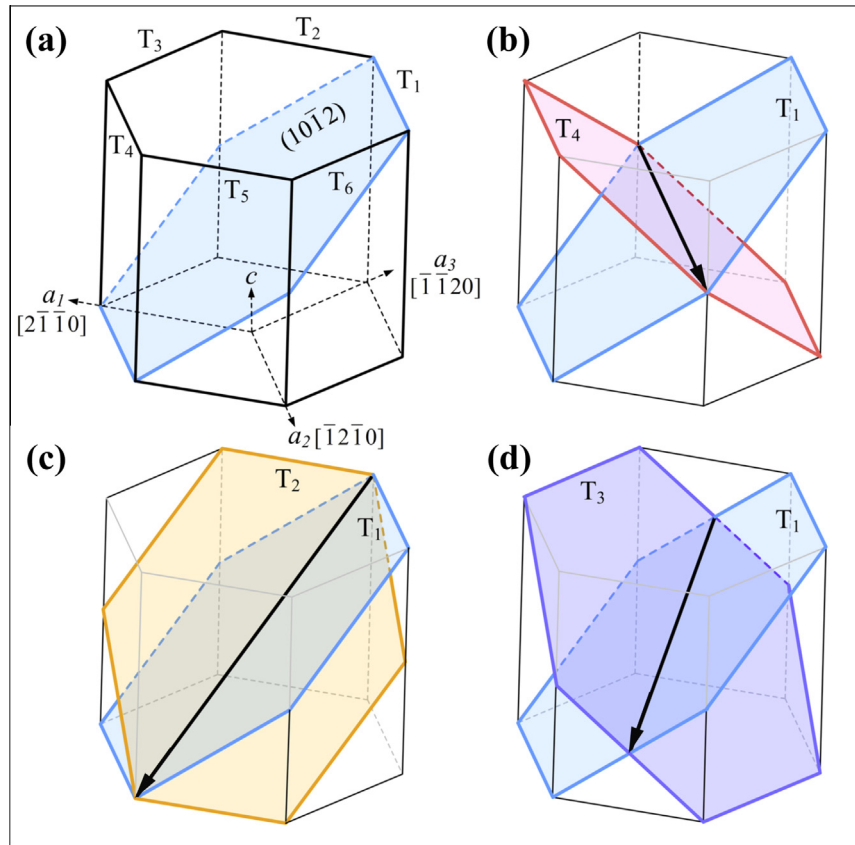
Fig. 1. (a) The six $\{10\bar{1}2\}\langle\bar{1}011\rangle$ twin variants T_i ($i = 1$–6) in an hcp structure can form three crystallographically different types of twin–twin interactions; (b) Type I twin–twin pair $T_4 \leftrightarrow T_1$ with the intersection line along $[\bar{1}2\bar{1}0]$, (c) Type II(a) twin–twin interaction $T_2 \leftrightarrow T_1$ with the intersection along $[\bar{2}\bar{2}43]$ and (d) Type II(b) twin–twin interaction $T_3 \leftrightarrow T_1$ with the intersection line along $[0\bar{2}\bar{2}1]$.

facilitate a discussion, we refer to the impinging twin as T_i. If the impinging twin T_i transmits into twin T_j, a secondary twin T_{jk} forms inside twin T_j.
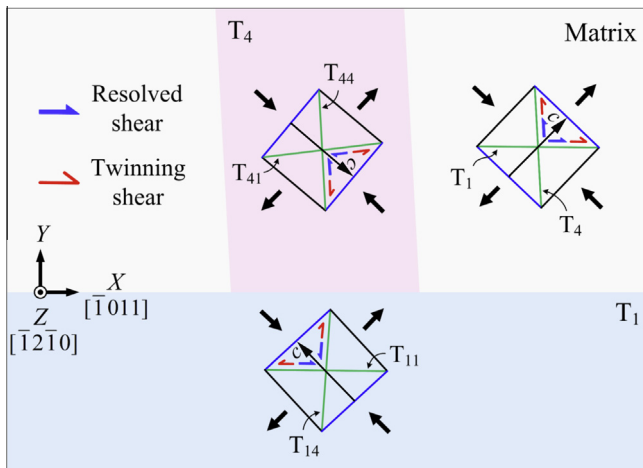

Fig. 2. A schematic of twin–twin interaction showing the relation between the direction of the resolved shear stress and the direction of twinning shear on the primary T_1 and T_4 twin planes, and on the $\{10\bar{1}2\}$ twinning planes inside twin T_1. The external loading in the figure favors primary twin growth but not secondary twin transmission when twin T_4 impinges on twin T_1.

Fig. 2 shows an impinging twin T_4 approaching a previously formed twin T_1. Both twins can be activated by the stress state depicted in Fig 2. Following Cahn's first constraint [42], the trace of the impinging twin is parallel to the intersection line between the two twins. The secondary twin could be either T_{11} or T_{14} inside twin T_1. For T_1 and T_4 we denote the direction of the resolved shear stress on the twinning plane with a blue arrow and the twinning shear direction with a red arrow. In the matrix they have the same direction (Fig. 2). The twinned crystal is rotated 86.3° about the zone axis with respect to the matrix and the c-axis experiences tension in the matrix and compression inside T_1. As a consequence, the direction of the resolved shear stress on the secondary twinning plane is opposite to the secondary twinning shear direction. Thus, the secondary twinning or twin transmission does not occur for Type I twin–twin interaction.

A more general analysis for Types I and II twin–twin interactions can be done using the Schmid criterion. Fig. 3a–d plots the Schmid factor (SF) of twins T_i ($i = 1\ldots4$) in an inverse pole figure for uniaxial tension acting on the parent hcp crystal. A positive SF (red domain) is associated with the stress directions that induce a resolved shear along the positive shear direction and activate T_i twinning. Take twin T_1 as an example. If the SF is negative (blue domains), T_1 is not activated by the corresponding
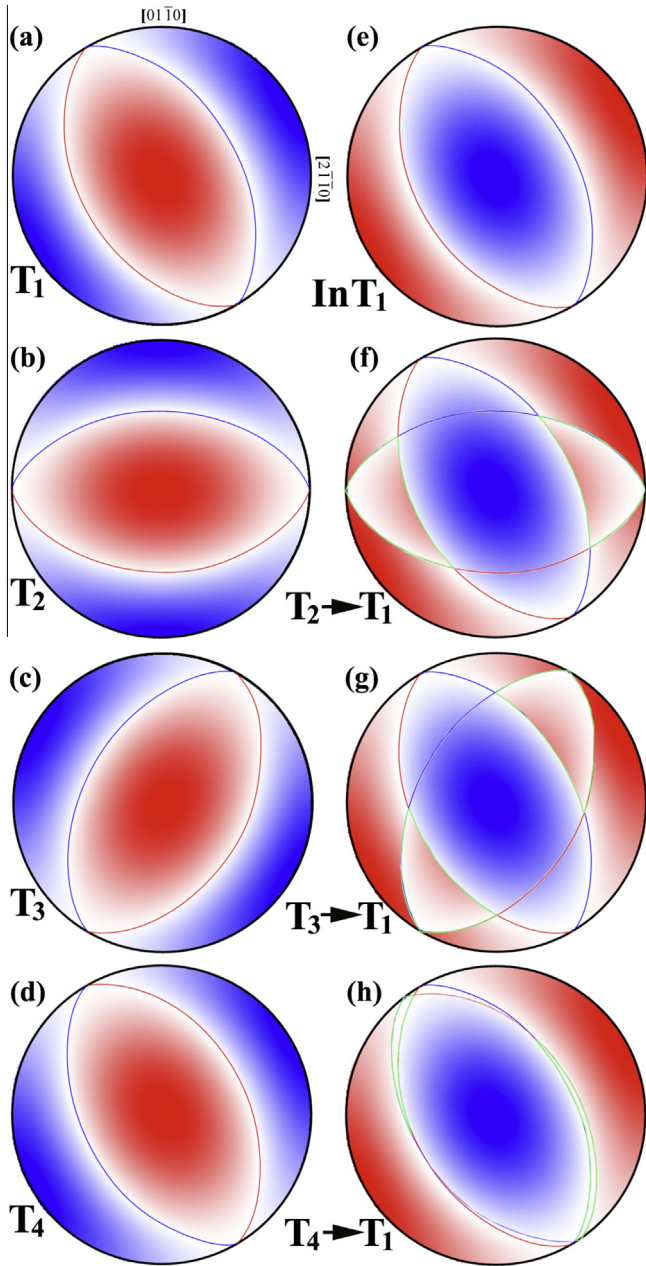
Fig. 3. Inverse pole figures of the Schmid factor of twinning systems associated with a tensile axis. Red identifies domains with positive resolved shear on twin system. Blue identifies negative resolved shear (no-twin-activation). Directions of potential activation stresses for activating: (a) twin T_1, (b) twin T_2, (c) twin T_3, (d) twin T_4, (e) twin T_1 after it has reoriented, (f) twin T_2 inside twin T_1, (g) twin T_3 inside twin T_1 and (h) twin T_4 inside twin T_1. The regions outlined by the green line represent the stress domain associated with the transmission of twin T_i into twin T_1. (For interpretation of the references to color in this figure legend, the reader is referred to the web version of this article.)

stress. Following reorientation of T_1, the *c*-axis reorients by nearly 90° and the SF of T_1 associated with the stress state changes sign (Fig. 3e) for the twinned crystal (from red to blue, and vice versa), meaning that the stress state that activated T1 cannot activate detwinning inside T_1. The following three cases correspond to Type I and II twins being able

to propagate inside T_1. Each of T_2, T_3 and T_4 is associated with positive and negative domains of SF in the parent crystal. To propagate from the original crystal into T_1 while being driven by the same stress, these twins have to exhibit non-empty intersections of positive domains when the I images in Fig. 3b–d are superposed with Fig. 3e, respectively. Such intersections are sketched in Fig. 3f–h as red regions. It should be noticed that while the same stress states allow T_2 and T_3 to propagate into T_1, the SFs associated with these domains are very low. In practice, we have not observed such a kind of twin–twin transmission. As for T_4 propagation into T_1 (Fig. 3h), the fact that the intersection of the red domains is practically null rules out such a propagation, which is also consistent with our experimental evidence.

2.3. Experimental observation of twin–twin structures

We performed two cyclic loading tests in Mg single crystal with respect to two different crystal orientations to study twin–twin structures. Using in situ optical microscopy (OM) and ex situ electron backscatter diffraction (EBSD) analysis, we observed twin–twin interactions and characterized microstructures resulting from twin–twin interactions.

A Mg single crystal was grown using the Bridgman method. A dog-bone specimen of gage length 5.0 mm and a square cross-section of 3.0 mm × 3.0 mm was fabricated using electric discharge machining. Under compression–tension cyclic loading along the $[10\bar{1}0]$ direction, twin variants $(10\bar{1}2)$ and $(\bar{1}012)$, sharing the $[1\bar{1}20]$ zone axis, have the maximum Schmid factor of 0.499 and are expected to be more active than the other four twin variants, which have a Schmid factor of 0.125. This offers the best situation to study the Type I co-zone twin–twin interaction. Under tension–compression cyclic loading along $[0001]$ direction, six twin variants, having identical Schmid factors of 0.499, are expected to be equally active. This is suitable for exploring both Type I and Type II twin–twin interactions. Before mechanical testing, the observation surface of the specimen was chemically polished using a solution of one part nitric acid, two parts hydrochloric acid and seven parts ethanol. The details of the mechanical testing setup can be found in Ref. [1].

For compression–tension test along the $[10\bar{1}0]$ direction, the specimen was prepared to have $X = [\bar{1}2\bar{1}0]$ $Y = [0001]$, and $Z = [10\bar{1}0]$, with the loading direction along the Z-axis. An EBSD scan on the specimen surface revealed that the $[10\bar{1}0]$ specimen is oriented close to the designed crystal orientations. The observation surface is the Y–Z plane. The specimen was initially loaded in compression to a strain of -0.75% and then unloaded slightly to a strain of -0.725% where we characterized the specimen surface by SEM and EBSD with an EBSD step size of 0.5 μm. The specimen was subsequently loaded under fully reversed strain-controlled compression–tension at a strain amplitude of 0.75%. During cyclic loading, the

morphological change of deformation twins was traced using in situ optical microscopy and the orientation of the twins was characterized based on EBSD analysis. For tension–compression tests in the $[0001]$ direction, the specimen was prepared to have $X = [10\bar{1}0]$, $Y = [\bar{1}2\bar{1}0]$ and $Z = [0001]$ with the loading direction along the Z-axis. An EBSD scan on the specimen surface revealed that the $[0001]$ specimen is oriented close to the designed crystal orientations. The observation surface is the Y–Z plane. The specimen was loaded for one cycle under fully reversed strain-controlled tension–compression with a strain amplitude of 0.5%. We characterized the specimen surface by SEM and EBSD with a scan resolution of 0.5 μm.

Through in situ OM and ex situ EBSD analysis, three microstructural features are observed in association with twin–twin interactions in the two specimens: (1) quilted-looking twin structure, (2) "apparent crossing" twin structure and (3) double twin structure. The quilted-looking twin structure forms through the propagation and blocking of multiple twin variants. This structure has been widely observed in materials with orthotropic [42–44], tetragonal [45] cubic [46,47], and hcp [35–40,48–51] crystal structures. Fig. 4a shows a quilted-looking twin structure in the specimen loaded along the $[10\bar{1}0]$ direction. The structure is composed of two twin variants, T_1 and T_4, that share the same zone axis. In the specimen loaded along the $[0001]$ direction, we observe six twin variants. Fig. 4b shows a quilted-looking twin structure composed of four twin variants, T_1, T_2, T_3 and T_5. It is noticed that the quilted-looking structure prevents the propagation and growth of twins in association with the formation of TTBs.

The crossing (or transmission) twin structure forms when an impinging twin crosses another twin through a secondary twinning path in the twinned crystal. Fig. 5 shows two "apparent crossing" twin structures. A closer observation reveals that neither twin actually crosses through the other twin, as we discuss below. Fig. 5a shows two T_1 twins and one T_2 twin. The crystal orientation in the intersection region has a c-axis misorientation angle of ∼6.2° with respect to the crystal orientation in the T_2 twin away from the twin–twin interaction, indicating that the crystal in the intersection region belongs to the T_2 twin but experiences a tilt induced by forming TTBs. In Fig. 5b, EBSD analysis shows three twins: two T_2 twins and one T_6 twin. The crystal orientation in the intersection region has a c-axis misorientation angle of ∼6.5° with respect to the crystal orientation in the T_6 twin away from the TTB, indicating that the crystal in the intersection region belongs to the T_6 twin but experiences a tilt induced by dislocation formation at the TTBs. These results clearly indicate that no twin crossing or transmission occurs upon the contact of one twin with another twin. This is different from the crossing twin structure in face-centered-cubic (fcc) structures [46,47] where twin transmission can occur under monotonic loading because the fcc structure exhibits three sets of twinning dislocations on each twinning plane [52–54]. The twinned crystal can be further twinned by the glide of twinning dislocations under the same stress condition. For hcp structures, a crossing twin structure is unlikely because twinning is unidirectional with one set of twinning dislocations per twinning plane. According to a Schmid analysis in Type I twin–twin interactions (Fig. 2), the twinned crystal cannot experience secondary twinning under the same stress because the twinning direction is opposite to the direction of the resolved shear stress in the twinned crystal. For Type II twin–twin interactions, the twinned crystal cannot be further twinned because the positive loading domains are characterized by very low Schmid factors (Fig. 3). Thus, crossing twin structures in hcp are unlikely as a result of twin–twin interaction. This is evidenced in our EBSD analysis where among all twin–twin structures we observed only "apparent crossing" twin structures without crossing twin structures. However, crossing twin structures could form if the local stresses depart substantially from the applied stress as a result of spatially distributed defects.

The double tensile twin structure is the one in which a tensile twin (or secondary twin) forms inside another tensile twin (or primary twin). There are two typical structures: one where the secondary twin does not connect another twin that interacts with the primary twin (Fig. 6a and b), and the other one is where the secondary twin does
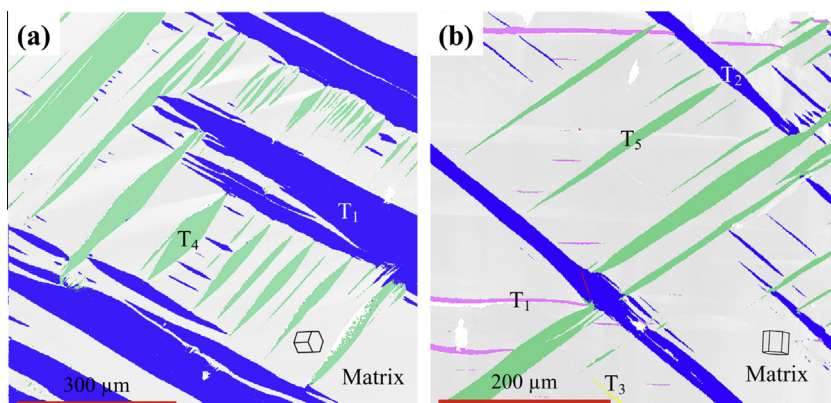

Fig. 4. Quilted-looking twin structures (a) in the specimen loaded along the $[10\bar{1}0]$ direction and (b) in the specimen loaded along the $[0001]$ direction.
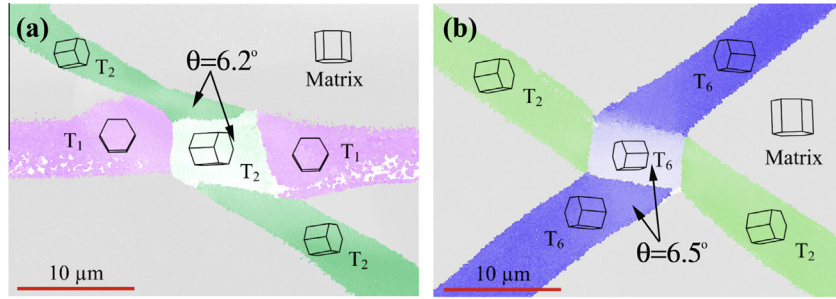
Fig. 5. "Apparent crossing" twin structures in the specimen loaded along the [0 0 0 1] direction: (a) two T_1 twins and one T_2 twin and (b) two T_2 twins and one T_6 twin.
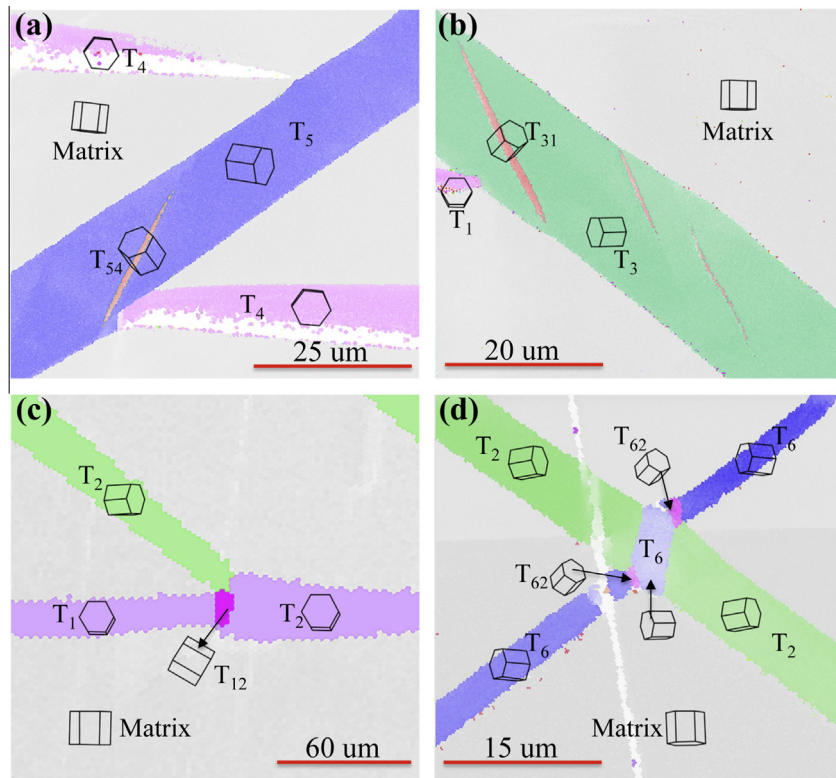

Fig. 6. Double tension twin structures in the specimen loaded along the [0 0 0 1] direction. Secondary twin does not connect to an incoming twin: (a) a secondary twin T_{54} inside a primary twin T_5 and (b) three secondary twins T_{31} inside a primary twin T_3. Secondary twin connects to TTBs: (c) a secondary twin T_{12} inside a primary twin T_1 and (d) two secondary twins T_{62} inside a primary twin T_6.

connect to another twin that interacts with the primary twin (Fig. 6c and d). Since secondary twins cannot occur inside a primary twin without changing the stress state in the primary twin, the double tensile twin structure can occur either due to a change in the applied loading or due to local stresses resulting from other defects such as an interacting twin.

3. Twin–twin boundaries

We have reported our observations of three types of twin–twin structures and briefly discussed the formation of these structures. In the following section, we address the formation mechanisms and microstructural characteris-

tics of these structures and their role in further twinning and detwinning based on EBSD analysis, crystallographic theory and dislocation theory.

3.1. Formation of TTBs

When one twin encounters another twin, TTBs form. Starting with Fig. 7a where an incoming twin T_i approaches the twin boundary of twin T_j, TTBs form through three possible mechanisms based on the reaction of twinning dislocations, as visualized in Fig. 7b–d.

The first mechanism corresponds to the impinging process (Fig. 7b) where the front tip of twin T_i is blocked at the boundary of twin T_j. TDs associated with twin T_i
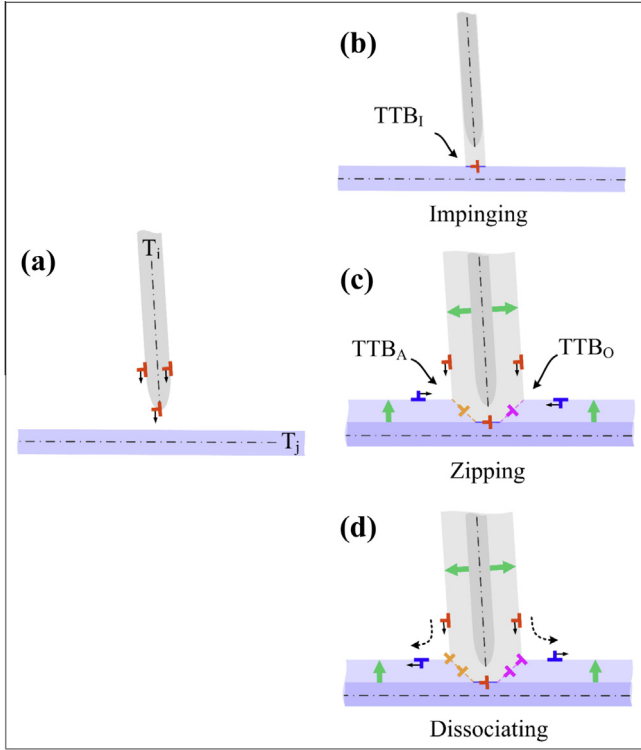
Fig. 7. Formation mechanisms of TTBs: (a) a twin T_i is approaching the boundary of a pre-existing twin T_j ($i \neq j$); (b) the impinging mechanism where TDs impinge on the T_j twin boundary, forming TTB$_I$; (c) the zipping mechanism where twinning dislocations associated with the two twins zip to form junctions; (d) the dissociating mechanism where a twinning dislocation associated with one twin dissociates into one twinning dislocation associated with the other twin and leaves one junction. The light gray and light blue domains correspond to the T_i and T_j twins, respectively. The TDs are drawn in red (T_i) and blue (T_j) colors. Orange and pink colors are used for resultant junctions (or TTB dislocations) due to TD reactions. According to the angles between two primary twinning planes, one TTB is referred to as TTB$_A$ (acute angle), and the other is referred to as TTB$_O$ (obtuse angle).

Fig. 8. Twin–twin boundary planes and Burgers vectors of boundary dislocations for the three twin–twin interactions: (a) Type I $T_4 \leftrightarrow T_1$ twin interaction; (b) Type II(a) $T_2 \leftrightarrow T_1$ twin–twin interactions; (c) Type II(b) $T_3 \leftrightarrow T_1$ twin–twin interactions.

impinge on the twin boundary of twin T_j. The TTB that forms between the two twins is referred to as TTB$_I$ where the subscript "I" refers to impinging. The TTB plane coincides with the T_j twinning plane and contains boundary dislocations that have the same character as the twinning dislocation associated with the incoming twin T_i.

The second and third mechanisms are associated with the growth of two twins, as shown in Fig. 7c and d. When both T_i and T_j grow through the glide of TDs, these TDs meet, react and form junctions. The pile-up of these junctions forms a dislocation wall, corresponding to the TTB. Two types of TTBs can form, as schematically shown in Fig. 7c and d. Based on the angles between the two primary twinning planes, one TTB is referred to as TTB$_A$ corresponding to an acute angle and the other is referred to as TTB$_O$ corresponding to an obtuse angle.

For the second mechanism, the formation of junctions is accomplished through zipping twinning dislocations associated with the two primary twins. The Burgers vector of the junction is thus equal to the sum of the two TDs. In
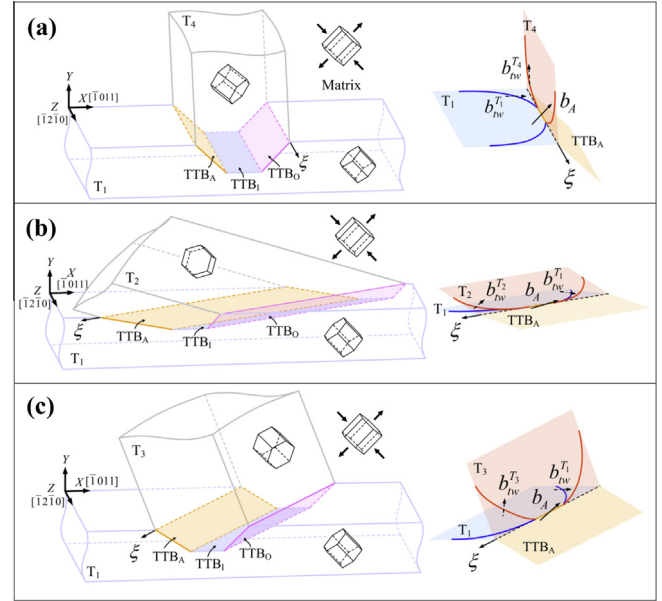
the case of a more common TTB that forms between an incoming T_4 twin and a T_1 twin, the line sense of all twinning dislocations is oriented along the $[1\bar{2}10]$ zone axis. The reaction process can be expressed as:

$$b_{tw}^{T_4} + b_{tw}^{T_1} \Rightarrow b_A$$
$$\lambda[10\bar{1}1] + \lambda[\bar{1}011] \Rightarrow 2\lambda[0001] \tag{1a}$$

and

$$b_{tw}^{T_4} + b_{tw}^{T_1} \Rightarrow b_o$$
$$\lambda[10\bar{1}1] + \lambda[10\bar{1}\bar{1}] \Rightarrow 2\lambda[10\bar{1}0] \tag{1b}$$

Note that $b_{tw}^{T_1}$ has Burgers vector $\lambda[\bar{1}011]$ at the left of twin T_4 and $\lambda[10\bar{1}1]$ at the right of twin T_4, where $\lambda = (3 - \kappa^2)/(3 + \kappa^2)$ ($\lambda = 0.064$ for Mg) and b_A and b_0 denote the Burgers vectors of the junctions in the TTBs TTB$_A$ and TTB$_O$, respectively.

In the third mechanism, the formation of TTBs is accomplished through dissociating the twinning dislocation of one twin into the twinning dislocation of the other twin plus a residual. As shown in Fig. 7d, a TD associated with T_i glides towards the boundary of the T_j and dissociates into a TD associated with twin T_j. The residual is left at the intersection of the two twins, corresponding to a junction. Taking $T_4 \rightarrow T_1$ twin pairs as example, the dissociation process can be expressed as:

$$b_{tw}^{T_4} + b_{tw}^{T_1} \Rightarrow b_A$$
$$\lambda[10\bar{1}1] + \lambda[10\bar{1}\bar{1}] \Rightarrow 2\lambda[0001] \tag{2a}$$

and

$$b_{tw}^{T_4} + b_{tw}^{T_1} \Rightarrow b_o$$
$$\lambda[10\bar{1}1] + \lambda[\bar{1}011] \Rightarrow 2\lambda[10\bar{1}0] \tag{2b}$$

Table 1
Burgers vectors of the dislocations on TTBs (TTB$_I$, TTB$_A$, TTB$_O$) for the three types of twin–twin interactions (all the vectors are described in the matrix crystal coordinate).

Twin pair	b_I	b_A	b_O	$2|b_I|^2/(\lambda a)^2$	$|b_A|^2/(\lambda a)^2$	$|b_O|^2/(\lambda a)^2$
$T_4 \leftrightarrow T_1$	$\lambda[10\bar{1}1]$	$2\lambda[0001]$	$2\lambda[10\bar{1}0]$	11.23	10.56	11.97
$T_2 \leftrightarrow T_1$	$\lambda[0\bar{1}11]$	$\lambda[\bar{1}\bar{1}22]$	$\lambda[1\bar{1}00]$	11.23	19.54	2.99
$T_3 \leftrightarrow T_1$	$\lambda[1\bar{1}01]$	$\lambda[0\bar{1}12]$	$\lambda[2\bar{1}\bar{1}0]$	11.23	13.54	9.00

Note: b_I, Burgers vector of dislocation impinged on a pre-existing twinning boundary; b_A and , Burgers vectors of dislocations on the TTB$_A$ and TTB$_O$ TTBs formed by reaction of TDs.

3.2. Configuration of TTBs

According to the three proposed mechanisms, we study here the crystallographic aspects of the TTBs, including boundary planes and boundary dislocations. Fig. 8 shows the three-dimensional geometry for the three twin–twin interactions. T_1 is the pre-existing twin. T_2, T_3 and T_4 are the incoming twins. The coordinate system ($OXYZ$) is fixed to the T_1 twinning plane. The X-axis aligns with the T_1 twinning shear direction $[\bar{1}011]$ and the Y-axis is normal to the T_1 twinning plane. The Z-axis points out-of-paper parallel to the $[1\bar{2}10]$ zone axis. Table 1 summarizes the Burgers vectors of junctions (or boundary dislocations) in the TTBs. b_I is the Burgers vector of the impinging TD associated with the incoming twin. b_A and b_o are the Burgers vectors that result from reaction of the TDs. The elastic energy associated with these dislocations is proportional to the square of the magnitude of Burgers vector and is computed for the three twin–twin interactions in Table 1. It is found that the formation of TTB$_A$ is energetically favorable while TTB$_O$ is unfavorable for Type I twin–twin interactions. Conversely, the formation of TTB$_O$ is energetically favorable while TTB$_A$ is unfavorable for Type II twin–twin interactions.

For example, the elastic energy associated with the left-hand side of Eqs. (1a) and (1b) is proportional to $11.23(\lambda a)^2$ for Type I twin interactions according to Frank's law [52]. The right-hand sides of Eqs. (1a) and (1b) are proportional to $10.56(\lambda a)^2$ and $11.97(\lambda a)^2$, respectively, indicating that the reaction is favorable for forming the TTB$_A$ boundary and unfavorable for forming the TTB$_O$ boundary when only considering the change in line energy of the dislocations. The change in the elastic energy associated with the dislocation dissociation (Eqs. (2a) and (2b)) increases, indicating that the dissociation mechanism is energetically unfavorable. However, the formation of dislocation walls will further reduce the net elastic energy due to the core–core interactions among these dislocations [52]. Thus both TTB$_A$ and TTB$_O$ boundaries could form through the two mechanisms.

The TTB plane is geometrically defined as a common interface bisecting two twinning planes. In practice, the TTB plane can be different because of thermodynamically driven reconstruction to minimize interface energy, such as faceted or curved interfaces [55–57]. Nevertheless, the net Burgers vector of the boundary dislocations is unchanged according to the Frank–Bilby theory [55–58] when the misorientation relationship between the two crystals remains unchanged. For a Type I co-zone twin–twin interaction, due to the twinning reorientation of the crystals, the boundary plane of TTB$_O$ bonds the basal planes in the two twins, which is referred to as BB. The boundary plane of TTB$_A$ bonds the prismatic planes in the two twins, as being referred to as PP. These structures have been examined recently using atomistic simulations in Mg [3]. The Burgers vector of the boundary dislocations is perpendicular to the TTB plane (Fig. 8a), forming a boundary dislocation tilt wall. Thus, TTB$_A$ and TTB$_o$ in Type I twin interactions can be characterized as low-angle symmetric tilt boundaries with a tilt angle of 7.4°.

For the Type II(a) twin–twin interaction, a crystallographic analysis according to a common interface bisecting two twinning planes shows that the boundary plane of TTB$_A$ is parallel to the $(11\bar{2}4)$ plane in the matrix and bonds the $(5\bar{2}\bar{3}6)$ plane in the T_1 twin and the $(\bar{2}5\bar{3}6)$ plane in the T_2 twin. The boundary plane of TTB$_O$ is parallel to the $(1\bar{1}00)$ in the matrix and bonds the $(\bar{1}2\bar{1}2)$ plane in the T_1 twin and the $(\bar{2}11\bar{2})$ plane in the T_2 twin. For Type II(b) twin–twin interactions, the boundary plane of TTB$_A$ is parallel to the $(01\bar{1}4)$ plane in the matrix and bonds the $(13\bar{5}\bar{8}6)$ plane in the T_1 twin and the $(\bar{13}856)$ plane in the T_3 twin. The boundary plane of TTB$_O$ is parallel to the $(2\bar{1}\bar{1}0)$ plane in the matrix and bonds the $(\bar{3}5\bar{2}14)$ plane in the T_1 twin and the $(\bar{3}25\bar{14})$ plane in the T_3 twin. As shown in Fig. 8b and c, the Burgers vector of the boundary dislocations has two components: one is perpendicular to the boundary plane and the other lies on the boundary plane and is not parallel to the intersection line (or junction line). Thus, TTB$_A$ and TTBo for Type II twin–twin interactions can be characterized to be tilt plus twist boundaries. The two bonded crystal planes in the two twins are of the same type but twisted relative to each other. It is worth mentioning that the geometrical definition results in the high index crystallographic planes.

TTBs associated with the Type I co-zone twin–twin interaction are observed from compressing the Mg single crystal in the $[10\bar{1}0]$ direction. Fig. 9a shows TTBs between a T_4 twin and a T_1 twin. Twin–twin boundaries consist of low-angle TTB$_O$ and TTB$_A$ tilt boundaries with a misorientation angle of 6.6° measured by EBSD. The
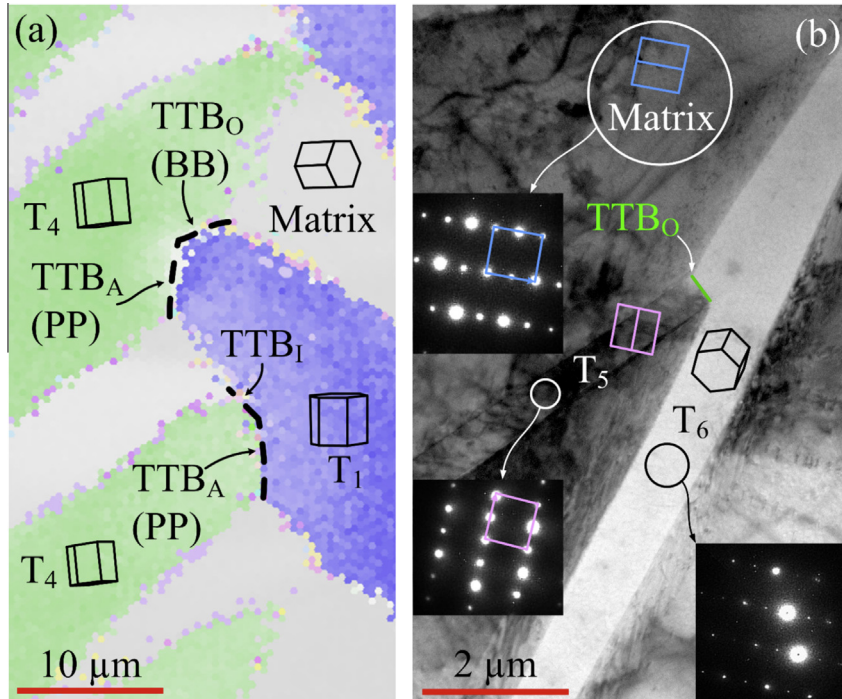
Fig. 9. Experimentally observed TTBs: (a) EBSD orientation map of low-angle TTBs, TTB_A (BB) and TTB_O (PP), in Type I co-zone twin interaction under compression in $[10\bar{1}0]$-Mg single crystal; (b) TEM bright field micrograph showing TTB_O in Type II(a) twin–twin interaction.

trace of the TTB_A boundary plane is close to traces of prismatic planes in both twins and referred to as PP boundary. The TTB_O boundary plane trace is approximately parallel to the basal plane traces in both twins and referred to as the BB boundary. Atomistic simulations of Type I co-zone twin interactions [3] with empirical potential for Mg have been used to examine the formation of PP and BB boundaries (see Supplementary Fig. S.1). Fig. 9b, a TEM bright field micrograph, shows a TTB_O boundary associated with Type II(a) twin–twin interactions. It is worth mentioning that no twin transmission is observed in either type of twin–twin interactions.

According to our experimental observations and theoretical analyses, $\{10\bar{1}2\}$ twins do not transmit into one another. The formation of the "apparent crossing" twin structures in Fig. 6c and d is addressed next using an argument based on the formation of TTBs. As shown in Fig. 10a, two T_i twins impinge on each side of a T_j ($j \neq i$) twin. Fig. 10b shows the formation of an "apparent crossing" twin structure accompanying the formation and growth of TTBs and the growth of the three twins. For generality, all kinds of TTBs are shown in Fig. 10b. In fact, different numbers or kinds of TTBs could form due to the local stresses and difference in the kinetics and energetics aspects for TTBs formation. For example, two types of TTBs are observed in Fig. 5a and one type of TTB is observed in Fig. 5b. Nevertheless, the intersection region visualized as the violet shaded area in Fig. 10b is part of twin T_j but tilted 6.4° from twin T_j due to boundary dislocations according to interface dislocation theory [52].

4. Influence of TTBs on twinning/detwinning

4.1. Influence on twinning

Once TTBs form, twinning dislocations associated with the incoming twin are blocked at the twin boundary and form boundary dislocations. Back-stresses resulting from the pile-up of these boundary dislocations hinder the motion of twinning dislocations toward the TTB, producing a stronger repulsion force near the TTB. Further growth and propagation of twins thus requires a high stress, resulting in strain hardening during twinning.

It is worth pointing out that for Type I twin–twin interactions, the two twinned crystals have a low misorientation angle of ∼7.4°. Thus, glide planes in both crystals are nearly parallel, and slip transmission for dislocation across TTBs is easy. For the easy basal slip in Mg, basal dislocation can transmit across TTB_O where the boundary plane is prismatic, forming a basal slip band. This has been observed in Mg [3]. For Type II twin–twin interactions, the two twinned crystals have large misorientation angles (>35°), and the traces of their glide planes with the boundary plane are not parallel, and thus slip transmission is difficult.

4.2. Influence on detwinning and secondary twinning

Under reversed loading, detwinning may occur as a reversal of the forming process. For interacting twins, TTB dislocations can dissociate into twinning dislocations
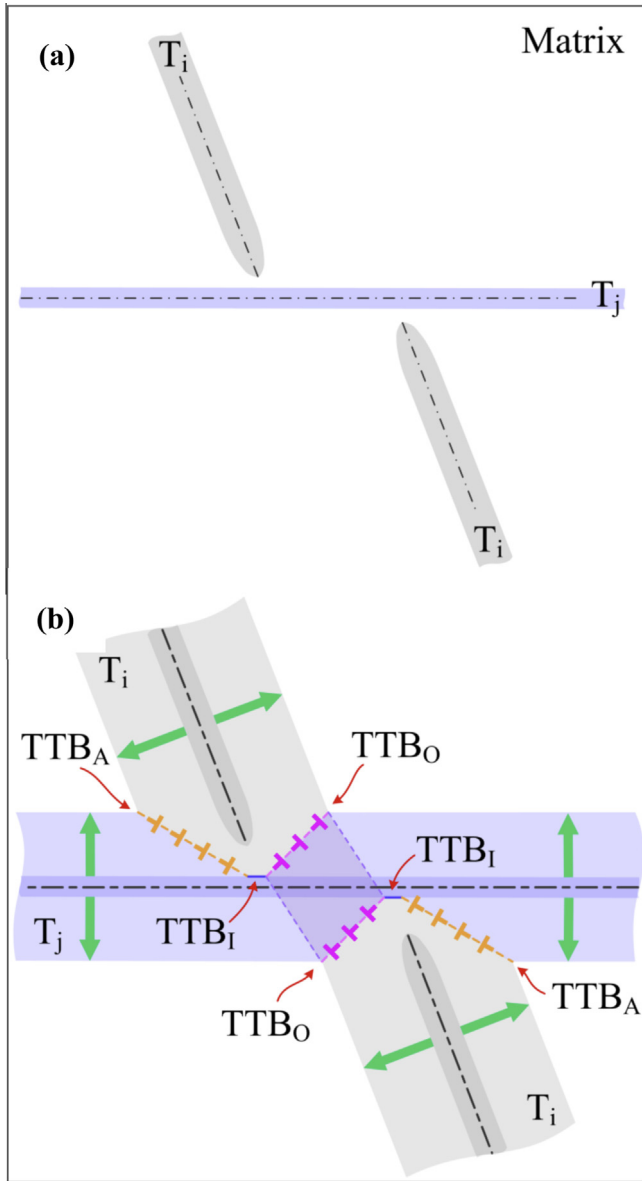
Fig. 10. Formation mechanisms of crossing-like twin structure: (a) a T_i twin encounters a pre-existing T_j twin from one side and another closely aligned parallel T_i twin contacts the same T_j twin from the other side ($j \neq i$); (b) Formation of TTBs at both sides of T_j twin via the zipping and/ or dissociating mechanisms. The dislocations on TTB_A and TTB_O are drawn in orange and pink colors, respectively. The green arrow indicates the direction of the twin boundary growth.
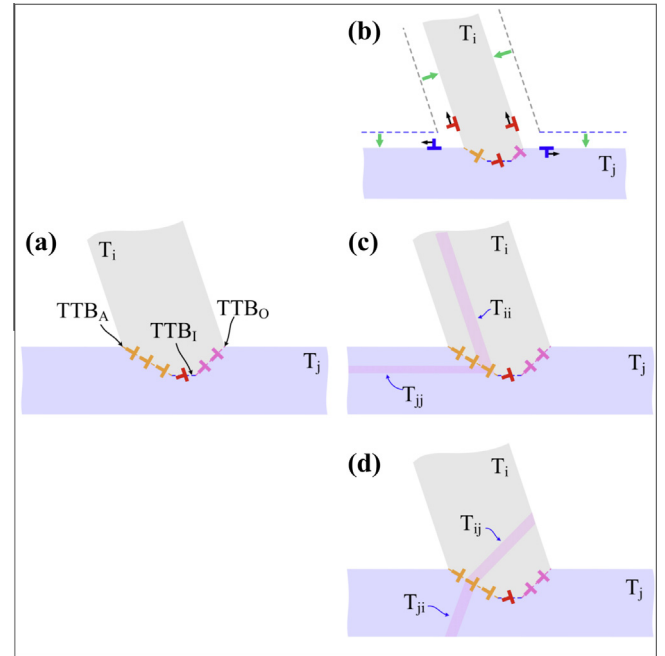

Fig. 11. Detwinning, re-twinning and double twinning mechanisms related to TTBs under reversed loading: (a) at the start of load reversal; (b) detwinning through dissociation of a single TTB dislocation into twinning dislocations; (c) secondary twinning with the same twin variant as the primary twin (or referred to as re-twinning) accompanying nucleation of twins from TTBs; (d) secondary twinning with a different twin variant from the primary twin (or referred to as double twinning) accompanying nucleation of twins from TTBs.

that glide on the twinning plane, causing the twin thickness to decrease (Fig. 11b). However, dissociation is an energetically unfavorable process based on the dislocation theory. It is expected that detwinning becomes more difficult with increasing loading cycles because more TTBs form that hinder detwinning. This is consistent with experimental measurements [1,2] and will be discussed later. More interestingly, secondary twins can propagate from TTBs, as observed in Fig. 6c and d. An EBSD analysis reveals two microstructural mechanisms, both based on secondary twins nucleating at and propagating from TTBs: (1) secondary twins leading to "detwinning from inside" (T_{ii} in

T_i and T_{jj} in T_j) (Fig. 6c) and (2) secondary twins where the secondary twin plane T_{ij} intersects with the primary twin planes T_i and T_j along the same intersection line.

Fig. 11 schematically illustrates possible deformation modes under reversed loading. Fig. 11a shows the general case of TTBs associated with the $T_i \rightarrow T_j$ twin interaction where three possible detwinning modes could operate. The first mode is associated with direct detwinning through dissociation/unzipping of boundary dislocations into twinning dislocations that glide on their associated twinning planes (Fig. 11b). This process can be expressed as:

$$b_{TTB} \Rightarrow b_{tw}^{T_i} + b_{tw}^{T_j} \tag{3}$$

The second and third detwinning modes are associated with nucleation and propagation of secondary twinning inside primary twins. In the second deformation mode (Fig. 11c), the secondary twin variant is either T_{ii} or T_{jj}, that is, the same variant is activated in primary. In the third deformation mode (Fig. 11d), the secondary twin variant is either T_{ij} or T_{ji}, that is, the variant of the other primary twin is active. Atomistic simulations and theoretical analysis [24] show that a minimum stable twin nucleus requires simultaneous nucleation of multiple twinning dislocations. Correspondingly, the second deformation mode can be expressed as:

$$nb_{TTB} \Rightarrow nb_{tw}^{T_{ii}} + nb_{tw}^{T_{jj}} \tag{4}$$

The third mode is similar to the second mode but with different reactions:

$$nb_{TTB} \Rightarrow nb_{tw}^{T_{ij}} + nb_r \tag{5a}$$

or

$$nb_{TTB} \Rightarrow nb_{tw}^{T_{ji}} + nb_r \tag{5b}$$

where n is equal to 3 for the normal-twinning mechanism [24]. nb_r is the residual dislocations left on the TTB. Compared to the first mode where detwinning is accomplished through successive dissociation of boundary dislocations, the second and third modes involve multiple dislocations and are less energetically favorable.

We further analyze the feasibility of the three deformation modes. For each dissociation process, we compute the interaction energy between the dissociated dislocations, the change in the elastic energy of the dislocations and the Schmid factor associated with the dissociated twinning dislocations. The results are summarized in Table 2. The Schmid factor for secondary twinning was computed for compression along the $[000\bar{1}]$ direction. It is clearly observed that (1) most of the dissociation processes are energetically unfavorable, resulting in a retarding behavior for detwinning and TTB-induced detwinning hardening; (2) the first mode (detwinning) is the easiest among the three modes;

and (3) secondary twinning is easiest for Type II(a) TTBs, and the most difficult for Type I co-zone TTBs.

4.3. Cyclic hardening of twinning/detwinning

When a Mg single crystal is subject to cyclic tension–compression loading along the [0001] direction, multiple twin variants are activated during the tensile stroke, and they tend to de-twin during the compressive reversal. Quilted-looking twin structures, "apparent crossing" twin structures and double twin structures form under these conditions and offer the best situation to study the influence of twin–twin interactions on hardening due to twinning and detwinning.

The [0001]-oriented Mg single crystal was subject to fully reversed strain-controlled tension–compression at a strain amplitude of 0.5% after the initial tensile loading and unloading. The cyclic stress vs. plastic strain is illustrated in Fig. 12a for several (up to 1610) hysteresis loops. The flow stresses for tension and compression increase with increasing number of loading cycles, corresponding to cyclic hardening. More importantly, the plastic strain accommodated by twinning/detwinning decreases with increasing number of loading cycles, indicating that twinning and detwinning become harder with increasing number of loading

Table 2

Dissociation process associated with three detwinning mechanisms, the energy associated with the dissociated secondary twin dislocation and the residual dislocation and the Schmid factor for secondary twinning under reversed loading in $[000\bar{1}]$ direction.

Dissociation	E_1	E_2	$E_1 - E_2$	$b_{tw}^{T_{ij}} \bullet b_r/(n\lambda a)^2$	m
Mechanisms 1 & 2: (n = 1 for Mechanism 1, n = 3 for Mechanism 2)					
Type I					
$nb_A \Rightarrow nb_{tw}^{T_{44}} + nb_{tw}^{T_{11}}$	10.56	11.23	0.67	−0.36	0.5
$nb_o \Rightarrow nb_{tw}^{T_{44}} + nb_{tw}^{T_{11}}$	11.97	11.23	−0.74	0.36	0.5
Type II(a)					
$nb_A \Rightarrow nb_{tw}^{T_{22}} + nb_{tw}^{T_{11}}$	19.54	11.23	−8.31	4.12	0.5
$nb_o \Rightarrow nb_{tw}^{T_{22}} + nb_{tw}^{T_{11}}$	2.99	11.23	8.24	−4.12	0.5
Type II(b)					
$nb_A \Rightarrow nb_{tw}^{T_{33}} + nb_{tw}^{T_{11}}$	13.54	11.23	−2.31	1.13	0.5
$nb_o \Rightarrow nb_{tw}^{T_{33}} + nb_{tw}^{T_{11}}$	9.00	11.23	2.23	−1.13	0.5
Mechanism 3 (n = 3)					
Type I					
$nb_I \Rightarrow nb_{tw}^{T_{41}} + nb_r (\text{or } nb_I \Rightarrow nb_{tw}^{T_{14}} + nb_r)$	5.62	17.59 (or 27.99)	11.97 (or 22.37)	−5.98 (or −11.19)	0.49
$nb_A \Rightarrow nb_{tw}^{T_{41}} (\text{or } nb_{tw}^{T_{14}}) + nb_r$	10.56	33.60	23.04	−11.55	0.49
$nb_o \Rightarrow nb_{tw}^{T_{41}} (\text{or } nb_{tw}^{T_{14}}) + nb_r$	11.97	33.60	21.63	−10.83	0.49
Type II(a)					
$nb_I \Rightarrow nb_{tw}^{T_{21}} + nb_r (\text{or } nb_I \Rightarrow nb_{tw}^{T_{12}} + nb_r)$	5.62	8.61 (or 7.01)	2.99 (or 1.39)	−0.266 (or −0.124)	0.12
$nb_A \Rightarrow nb_{tw}^{T_{21}} (\text{or } nb_{tw}^{T_{12}}) + nb_r$	19.54	12.64	−6.90	3.43	0.12
$nb_o \Rightarrow nb_{tw}^{T_{21}} (\text{or } nb_{tw}^{T_{12}}) + nb_r$	2.99	12.64	9.65	−4.82	0.12
Type II(b)					
$nb_I \Rightarrow nb_{tw}^{T_{31}} + nb_r (\text{or } nb_I \Rightarrow nb_{tw}^{T_{13}} + nb_r)$	5.62	14.64 (or 18.22)	9.02 (or 12.60)	−4.49 (or −6.29)	0.12
$nb_A \Rightarrow nb_{tw}^{T_{31}} (\text{or } nb_{tw}^{T_{13}}) + nb_r$	13.54	23.85	10.31	−5.16	0.12
$nb_o \Rightarrow nb_{tw}^{T_{31}} (\text{or } nb_{tw}^{T_{13}}) + nb_r$	9.00	23.85	14.85	−7.42	0.12

Note: b_I, Burgers vector of the impinged twinning dislocation on the T_1 twin boundary; b_A, Burgers vector of the TTB$_A$ boundary dislocation; b_o, Burgers vector of the TTB$_O$ boundary dislocation; $b_{tw}^{T_{ij}}$, Burgers vector of the dissociated secondary twinning dislocation; b_r, Burgers vector of the dissociated residual dislocation; m, Schmid factor for secondary twinning under reversed loading in the $[000\bar{1}]$ direction. $E_1 = |b_{TTB}|^2/(n\lambda a)^2$ and $E_2 = (|b_{tw}^{T_{ij}}|^2 + |b_r|^2)/(n\lambda a)^2$.
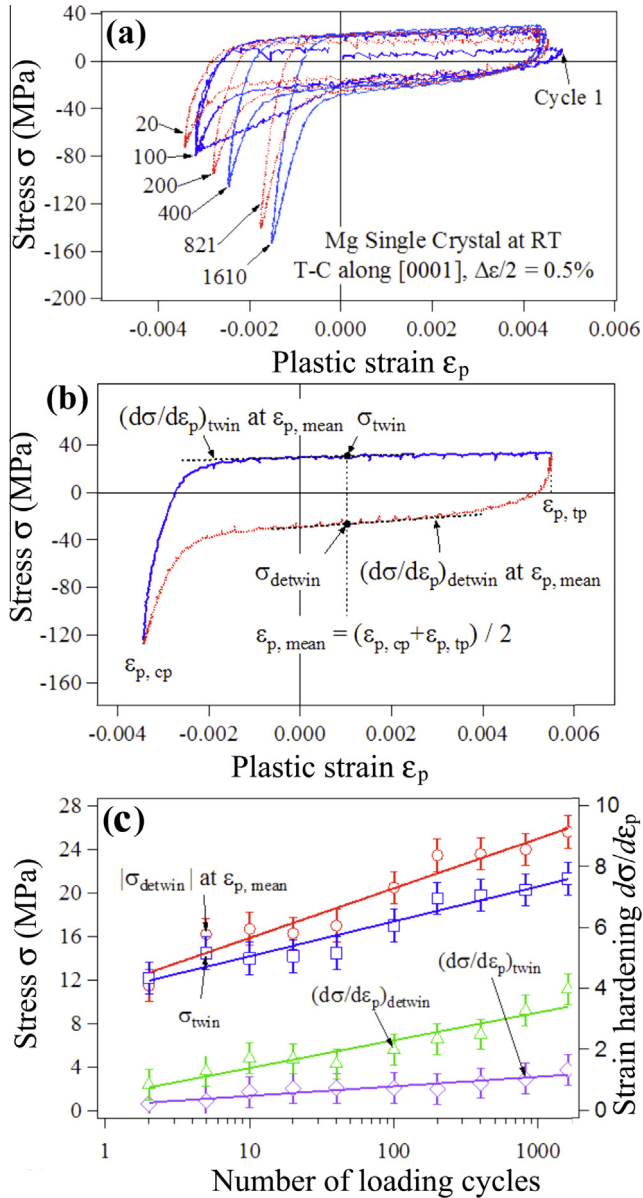
Fig. 12. Cyclic hardening of the [0001]-oriented Mg single crystal subjected to fully reversed tension–compression at a strain amplitude of 0.5%: (a) stress–plastic strain hysteresis loops from the first to the 1610th loading cycle; (b) twinning stress (σ_{twin}), detwinning stress ($|\sigma_{detwin}|$) and their corresponding plastic moduli ($(d\sigma/d\varepsilon_p)_{twin}$ and $(d\sigma/d\varepsilon_p)_{detwin}$) at the mean plastic strain ($\varepsilon_{p,mean}$)) as indicated in a typical stress–plastic strain hysteresis loop; (c) variation of twinning stress, detwinning stress and their corresponding plastic moduli with the number of loading cycles.

plastic strain and the compressive peak plastic strain in each loading cycle. The mean flow stress is the stress corresponding to the mean plastic strain for each cycle. The mean hardening rate is the slope of the stress–strain curve at the mean plastic strain. For each full loading cycle we compute the mean twinning stress, the mean detwinning stress and the mean strain hardening rates. The results clearly show two hardening features (Fig. 12c): the mean stress and hardening rate during detwinning are greater than those associated with twinning and both of them increase with the number of cycles. The higher flow stress for detwinning can be mainly attributed to the energetically unfavorable dissociation of TTBs, which require a higher stress to be reversed. The increasing flow stress with loading cycles can be mainly attributed to the accumulation of un-reversed TTBs and the formation of secondary twins. During twinning, twinning dislocations associated with the impinging twin are blocked at the pre-existing twin boundary, and quilted-looking twin structures form (also see Fig. 2 in Ref. [1]). A backstress then results from the pile-up of these boundary dislocations and will hinder the motion of twinning dislocations toward the TTB, producing a stronger repulsion force near the TTB. The further growth and propagation of twins thus require a high stress, corresponding to strain hardening during twinning. During detwinning, in addition to the effect due to energetically unfavorable dissociation, more secondary twins form at TTBs as the loading cycles increase. The nucleation and growth of secondary twins tends to suppress detwinning of the primary twin because the plastic deformation associated with secondary twinning decreases the local stress [59]. Thus, the mean stress and mean strain hardening rate during detwinning increase more rapidly than those during twinning.

Two other possible strain hardening mechanisms to be considered during cyclic loading are: (1) the lattice re-orientation of the twinned domains into "hard" orientations; (2) the accumulation of dislocations with each cycle. The latter is more likely to be present in polycrystalline aggregates, or in single crystals oriented for multiple slip, or when the cyclic strain amplitude is large. Neither of these conditions applies to our test. We performed fatigue on single crystal where the normal stress is either perpendicular or parallel to the basal plane in the twin and matrix domains, respectively. As a consequence, basal slip is unlikely to make a significant contribution to deformation during tension or compression due to a low or zero Schmid factor. In addition, the stress magnitude is lower than 40 MPa during the tensile stroke and unlikely to activate non-basal slip. The fact that the stress remains fairly flat throughout the tensile stroke in every cycle indicates that twinning is the dominant deformation mode and that non-basal slip inside the "hard" twinned domains is not active. The flow stress is also flat during most of the compressive stroke, when detwinning takes place, but increases at the end, a fact that which we attribute to the activation of pyramidal slip inside the de-twinned crystal. However, at these low cyclic plastic

cycles, and more strain is accommodated elastically. The sharp increase in the flow stress at the end of the compression loading reversal can be attributed to the exhaustion of easy detwinning followed by activation of hard pyramidal slip, since the de-twinned crystal is not oriented for basal slip activation.

In order to quantify the effect of twinning and detwinning upon cyclic hardening, we define a mean flow stress and a mean hardening rate as follows (Fig. 12b). A mean plastic strain is computed as the average of the tensile peak
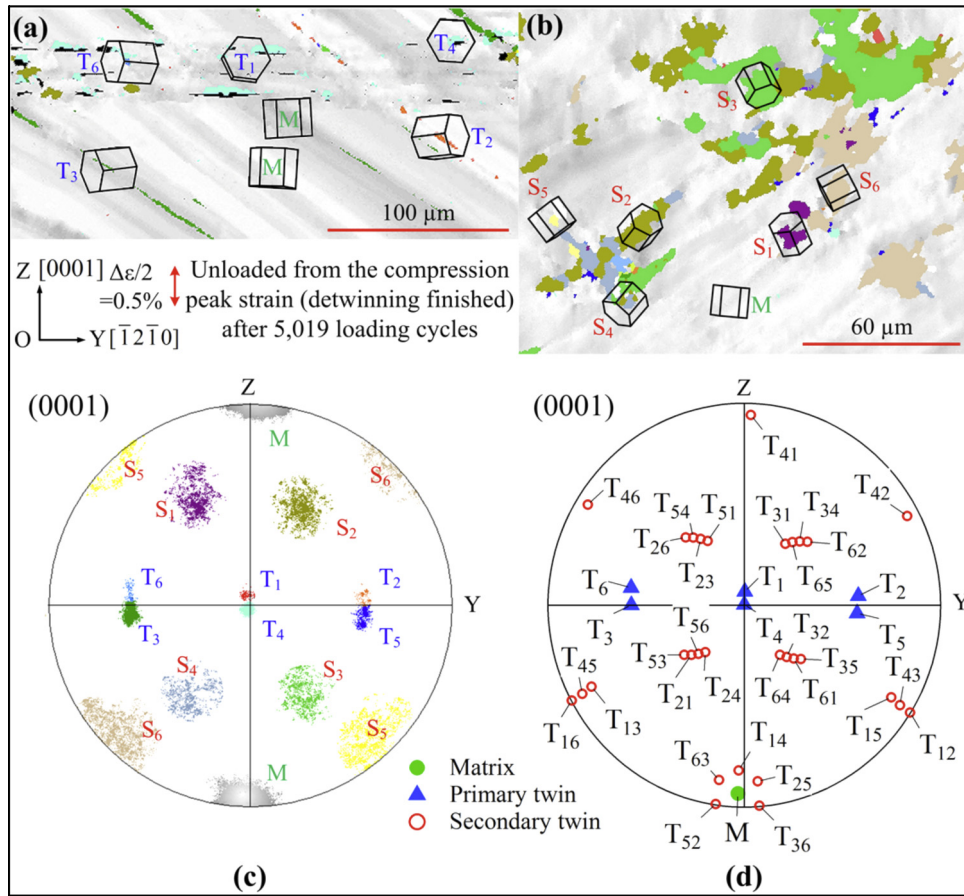
Fig. 13. (a) Low-magnification crystal orientation map showing primary twins and (b) secondary twins. (c) Discrete (0 0 0 1) pole figure from the EBSD scan with the pole regions highlighted in different colors; (d) calculated (0 0 0 1) pole figure for the original matrix (M), primary tensile twins (T_i, $i = 1,2,3...6$), and secondary tensile twins (T_{ij}, $i, j = 1,2,3...6$) with respect to the primary tensile twins.

strains ($\varepsilon < 0.005$) any dislocation generated will be most likely annihilated during unloading upon strain reversal, and twinning will be the dominant deformation mode for the rest of the tensile stroke. As a consequence, strain hardening is therefore mainly attributed to TTB interactions and to the build-up of secondary twins.

The phenomenon of secondary twin formation is documented in Fig. 13, and we believe that it plays a role in the hardening process associated with twinning/detwinning. Fig. 13a is a low-magnification crystal orientation map with different areas corresponding to the residual primary twins. Fig. 13b is a higher magnification crystal orientation map showing where secondary twins have been activated. Fig. 13c is the discrete (0 0 0 1) pole figure based on the EBSD scan (one point per pixel) with the separate crystal orientations highlighted in different colors. The sample was unloaded from the compressive peak strain (detwinning finished) after 5019 loading cycles. Based on the initial parent/matrix orientation, Fig. 13d shows the calculated position of (0 0 0 1) poles following primary and secondary twinning for all variant combinations. A comparison of Fig. 13c with Fig. 13d confirms that secondary twinning is active during the cyclic loading (see Regions S1–S6 in Fig. 13c).

5. Conclusions

Mg and Mg alloys exhibit limited formability at room temperature because their hcp structures have a limited number of easy slip systems. Consequently, twinning plays a critical role in plastic deformation, and twinning/detwinning is active during strain path changes, of which cyclic loading is an extreme case. $\{\bar{1}012\}$ twinning/detwinning is the most commonly activated twinning mode. Depending on grain orientation and loading conditions, multiple twin variants interact with each other, consequently forming quilted-looking twin structures, crossing-like twin structures and double twin structures. Twin–twin interactions and the microstructures that they generate are found to correlate with mechanical hardening. We studied twin–twin interactions by combining experimental observations and theoretical analysis. The major conclusions of this work are:

(1) According to a crystallographic analysis, twin–twin interactions can be classified into two types: Type I corresponding to two twins that share a $\langle 11\text{–}20 \rangle$ zone axis and Type II interactions that share a different zone axis.

(2) When loading favors the growth of the two twins, one twin cannot transmit into the other across a twin boundary through the secondary twinning path. Consequently, TTB forms.

(3) According to Schmid analysis, for a Type I twin–twin interaction, the same loading condition activates either twinning or detwinning of both twins, and twin transmission cannot occur. For Type II twin–twin interactions, twinning or detwinning of both twins can be activated under some loading conditions, and in some cases twinning is activated for one twin while detwinning is activated for the other. However, twin transmission is unlikely. Of all twin–twin structures observed in our EBSD experiments, crossing twin structures were not observed.

(4) A TTB can form through three mechanisms: impinging, zipping, and dissociating of twinning dislocations. All of these create twin–twin-boundary dislocations. For a Type I twin–twin interaction, the TTB is a low angle tilt boundary with the habit plane being parallel either to the basal or the prismatic planes in each twin. For Type II twin–twin interactions, the TTB adopts a high index crystallographic plane according to geometry analysis and could thus evolve to be a complex boundary following thermodynamic relaxation. Twin–twin boundary dislocations can be characterized by reactions of twinning dislocations associated with the two twin variants.

(5) "Apparent crossing" twin structures are a result of TTB formation. The crystal in the intersection region experiences a tilt induced by the pile-up of TTB dislocations.

(6) Under reversed loading, detwinning is hindered because of the energetically unfavorable dissociation of TTB dislocations. Most interestingly, secondary twinning can be activated at Type II TTBs under reversed loading.

(7) Under cyclic loading, three kinds of twin structures (quilted-looking, "apparent crossing", and double tensile twin or secondary twins) form as a consequence of twin–twin interactions. These microstructures correlate with the observed cyclic hardening due to twinning and detwinning.

Acknowledgements

Appendix A. Supplementary data

Supplementary data associated with this article can be found, in the online version, at http://dx.doi.org/10.1016/j.actamat.2014.05.030.

References

[1] Yu Q, Zhang J, Jiang Y. Philos Mag Lett 2011;91:757.
[2] Yu Q, Wang J, Jiang Y. J Mater 2013;2013:903786.
[3] Yu Q, Wang J, Jiang Y, McCabe RJ, Tomé CN. Mater Res Lett 2013;2:82.
[4] Lou X, Li M, Boger R, Agnew S, Wagoner R. Int J Plast 2007;23:44.
[5] Li Y, Enoki M. Mater Sci Eng A 2012;536:8.
[6] Clausen B, Tomé CN, Brown DW, Agnew SR. Acta Mater 2008;56:2456.
[7] Wu L, Jain A, Brown DW, Stoica GM, Agnew SR, Clausen B, et al. Acta Mater 2008;56:688.
[8] Wang H, Wu PD, Tomé CN, Wang J. Mater Sci Eng A 2012;555:93.
[9] Wang H, Wu PD, Wang J. Int J Plast 2013;47:49.
[10] Wang H, Wu PD, Wang J, Tomé CN. Int J Plast 2013;49:36.
[11] Proust G, Tomé CN, Jain A, Agnew SR. Int J Plast 2009;25:861.
[12] Beyerlein IJ, Wang J, Barnett MR, Tomé CN. Proc R Soc A Math Phys. Eng Sci 2012;468:1496.
[13] Beyerlein IJ, Capolungo L, Marshall PE, McCabe RJ, Tomé CN. Philos Mag 2010;90:2161.
[14] Beyerlein IJ, McCabe RJ, Tome CN. J Mech Phys Solids 2011;59:988.
[15] Yu Q, Zhang J, Jiang Y. Mater Sci Eng A 2011;528:7816.
[16] Yin SM, Yang HJ, Li SX, Wu SD, Yang F. Scr Mater 2008;58:751.
[17] Wang L, Yang Y, Eisenlohr P, Bieler TR, Crimp MA, Mason DE. Metall Mater Trans A 2009;41:421.
[18] Khosravani A, Scott J, Miles MP, Fullwood D, Adams BL, Mishra RK. Int J Plast 2013;45:160.
[19] Ye J, Mishra RK, Sachdev AK, Minor AM. Scr Mater 2011;64:292.
[20] Liu L, Wang J, Gong SK, Mao SX. Phys Rev Lett 2011;106:175504.
[21] Zhang XY, Li B, Wu XL, Zhu YT, Ma Q, Liu Q, et al. Scr Mater 2012;67:862.
[22] Tu J, Zhang X, Wang J, Sun Q, Liu Q, Tomé CN. Appl Phys Lett 2013;103:051903.
[23] Morrow BM, McCabe RJ, Cerreta EK, Tomé CN. Metall Mater Trans A 2014;45:36.
[24] Wang J, Hirth JP, Tomé CN. Acta Mater 2009;57:5521.
[25] Li B, Ma E. Acta Mater 2009;57:1734.
[26] Wang J, Hoagland RG, Hirth JP, Capolungo L, Beyerlein IJ, Tomé CN. Scr Mater 2009;61:903.
[27] Wang J, Beyerlein IJ, Tomé CN. Scr Mater 2010;63:741.
[28] Wang J, Beyerlein IJ, Hirth JP, Tomé CN. Acta Mater 2011;59:3990.
[29] Wang J, Beyerlein IJ, Hirth JP. Model Simul Mater Sci Eng 2012;20:024001.
[30] Wang J, Liu L, Tomé CN, Mao SX, Gong SK. Mater Res Lett 2013;1:81.
[31] Wang J, Yadav SK, Hirth JP, Tomé CN, Beyerlein IJ. Mater Res Lett 2013;1:126.
[32] Wang J, Yu Q, Jiang Y, Beyerlein IJ. JOM 2014;66(1):95–101.
[33] Wang J, Beyerlein IJ, Tomé CN. Int J Plast 2014;56:156–72.
[34] Serra A, Bacon DJ. Philos Mag A 1996;73:333.
[35] Reed-Hill R, Buchanan E. Acta Metall 1963;11:73.
[36] Jiang L, Jonas J, Luo A, Sachdev A, Godet S. Mater Sci Eng A 2007;445–446:302.
[37] Oppedal AL, El Kadiri H, Tomé CN, Kaschner GC, Vogel SC, Baird JC, et al. Int J Plast 2012;30–31:41.
[38] El Kadiri H, Kapil J, Oppedal AL, Hector LG, Agnew SR, Cherkaoui M, et al. Acta Mater 2013;61:3549.
[39] Pratt PL. Acta Metall 1953;1:692.
[40] Roberts E, Partridge PG. Acta Metall 1966;14:513.
[41] Choi S-H, Kim JK, Kim BJ, Park YB. Mater Sci Eng A 2008;488:458.
[42] Cahn RW. Acta Metall 1953;1:49.
[43] Xin Y, Wang M, Zeng Z, Nie M, Liu Q. Scr Mater 2012;66:25.
[44] Fernández A, Jérusalem A, Gutiérrez-Urrutia I, Pérez-Prado MT. Acta Mater 2013;61:7679.
[45] Maruyama S, Kiho H. J Phys Soc Jpn 1956;11:516.

[46] Mahajan S, Chin GY. Acta Metall 1974;22:1113.
[47] Rajan K. J Mater Sci Lett 1982;1:482.
[48] Nave M, Barnett M. Scr Mater 2004;51:881.
[49] Hong S-G, Park SH, Lee CS. Scr Mater 2011;64:145.
[50] Jäger A, Ostapovets A, Molnár P, Lejček P. Philos Mag Lett 2011;91:537.
[51] Zhang L, Han Y. Mater Sci Eng A 2009;523:130.
[52] Hirth JP, Lothe J. Theory of dislocations. Melbourne, FL: Krieger; 1992.
[53] Wang J, Huang H. Appl Phys Lett 2006;88:203112.
[54] Wang J, Beyerlein IJ, Mara NA, Bhattacharyya D. Scr Mater 2011;64:1083.
[55] Hirth JP, Pond RC, Hoagland RG, Liu X-Y, Wang J. Prog Mater Sci 2013;58:749.
[56] Wang J, Hirth JP, Pond RC, Howe JM. Acta Mater 2011;59:241.
[57] Kang K, Wang J, Beyerlein IJ. J. Appl. Phys. 2012;111:53531.
[58] Bilby BA, Bullough R, Smith E. Proc R Soc A Math Phys. Eng Sci 1955;231:263.
[59] Xiong X, Yu Q, Jiang Y. Int J Plast 2014;53:107–24.